ORIGINAL RESEARCH ARTICLE

Improving Surface Structures of Al-Doped Zinc Oxide Thin Films to Apply in CO Gas-Sensing Property by Designing Processes Through RF Magnetron Sputtering

Shao-Hwa Hu[1] · Yen-Sheng Lin[2] · Shui-Hsiang Su[2] · Jing-Shi He[1] · Ya-Zhao Ai[1]

Abstract

Because of their favorable sensitivity in chemical environments, zinc oxide (ZnO) materials are widely used in gas sensing. This study performed deposition of aluminum-doped ZnO nanofilms through radiofrequency magnetron sputtering. Oxygen flux and power during sputtering were altered to adjust the films' surface morphology, produce a highly porous structure, and increase sensitivity to carbon monoxide. For sensitivity testing, the film was encapsulated in a gas sensor by sputtering copper electrodes and fixing wires to the copper electrodes with silver glue. Field-emission scanning electron microscopy and x-ray diffractometry were used to analyze the films' surface microstructure and crystallinity. Ultraviolet–visible spectrophotometry was used to measure the film surface's light absorbance and porousness. Sensitivity to carbon monoxide (CO) under lower temperatures was tested using our gas-sensing circuitry, which involves a Keithley 2400 source meter used to monitor changes in impedance in real time. The results demonstrate that an oxygen flux of 10 sccm and sputtering power of 175 W produced films with favorable surface morphology and increased the maximum CO response value. Thus, the surface structure of the films can be adjusted by optimizing sputtering parameters, which increases sensitivity to CO gas reactions. This study demonstrated the films' potential application in gas sensors.

Introduction

Rapid technological advancement has exacerbated human effects on the environment, particularly those of industrial development, thermal power generation, and automobile dependency. To maintain ecological equilibrium and ensure the health and safety of the human population, the detection of harmful gases has become imperative. Carbon monoxide (CO) and methane are examples of undetectable lethal gases because they are colorless and odorless. The most lethal part of a fire is the CO and carbon dioxide it generates.[1–3] When indoor water heaters have incomplete combustion, they generate CO, which is incredibly dangerous because it bonds with red blood cells and reduces the ability of blood to carry oxygen. The resulting lack of oxygen to tissues in the body produces symptoms of CO poisoning. The research and development of gas sensors can help detect and minimize harm as quickly as possible. The first gas sensor was created in 1923 and involved heating tin dioxide (SnO_2) to several hundred degrees Celsius with a platinum wire and using catalysis to detect a target gas in the air. Nowadays, semiconductor CO sensors are most frequently used.[4–6] Unlike earlier models, semiconductor CO sensors operate not through a direct reaction between CO and a metal oxide, such as zinc oxide (ZnO) but by reacting with the surrounding oxygen; this slight difference in the detection process increases the sensor's lifespan. Because metal–oxide–semiconductor (MOS) CO sensors are low cost and can be miniaturized and mass produced, they may be applicable as wearable devices; thus, research on semiconductor CO sensor technology has begun to receive attention. Gas sensors come in a wide range of models that operate under various principles and can be grouped into five categories: semiconductor sensors, infrared
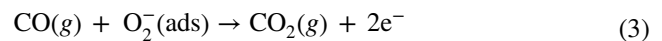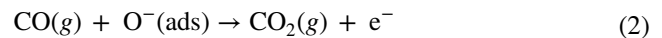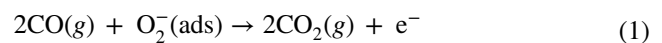
✉ Yen-Sheng Lin
  yslin@isu.edu.tw

1 Dongguan Polytechnic, Dongguan, Guangdong, China

2 Department of Electronic Engineering, I-Shou University, Kaohsiung, Taiwan, ROC

absorption sensors, electrochemical sensors, thermal conductivity detectors, and catalytic combustion sensors.[7–9] Semiconductor gas sensors can be further divided into *n*-type and *p*-type semiconductors. CO sensors on the market are mainly electrochemical. To lower costs and expand production to a mass scale, research teams have increasingly invested in the development of semiconductor gas sensors, which have high response values and low production costs and can be easily combined with other components to form a gas detection device. These characteristics enable the design and structure of a gas detector to be streamlined.[10–12] Thus, semiconductor gas sensors are more applicable than conventional optical gas sensors and chemiresistive-type sensors. Semiconductor gas sensors are based on conductivity, which changes in response to gas absorbance (in this case, the redox reaction). Unsaturated oxygen levels produce unbonded free electrons, creating electron holes in the aluminum-doped ZnO (AZO) lattice.[13,14] When gas molecules or atoms attach to the surface of AZO, an *n*-type semiconductor, the release or absorbance of electrons as a result of the redox reaction can increase or decrease the density of electron holes and thereby alter the electrical impedance value. This change in impedance value enables the detection of gas reactions.[15–18] This detection mainly involves the semiconductor surface-type reaction, so the structural shape and surface morphology of the semiconductor are very important. Semiconductor sensors have been widely researched and applied to the detection of toxic gases.[19–21] The parameters that affect surface absorbance are the surface structure and the composition of the metal oxide film. Changing a film from a two-dimensional metal oxide to a three-dimensional metal oxide or doping the surface of the metal oxide with catalytic elements[22–24] can increase film sensitivity and selectivity. However, doping complicates the gas-sensing mechanism so that the main cause of improved sensor characteristics will not be easily identified.[25,26] MOS sensors can be *p*-type or *n*-type sensors. Common *p*-type sensor materials include ceric oxide, nickel oxide, and cupric oxide. Common *n*-type sensor materials are ZnO, indium oxide (In_2O_3), and SnO_2. Gas sensors made from these materials, such as AZO, In_2O_3, and ZnO[27–30], have demonstrated favorable sensitivity in gas sensing.[31–35] In 1991, Chaonan et al. discovered that reducing the grain size of a material benefits the gas-sensing response by increasing its value.[36–38] Research has revealed that, when the SnO grain size decreases, the gas-sensing effect improves. Chaonan et al. also proposed a model for examining the effects of grain size on gas sensing, with *D* as the grain size and *L* as the thickness of the depletion region of the material surface.[39–41] When the grain size is much larger than twice the thickness of the depletion region, the electrical changes caused

by the depletion region are negligible, resulting in a low response value.[42–44] When *D* was substantially greater than or equal to 2*L*, the electrical changes caused by the depletion region were more pronounced. When *D* was less than 2*L*, the electrical change caused by the depletion region occupied the majority of the material and resulted in a considerable change in the response value. In a 2012 study on the CO-sensing properties of flower-like ZnO microstructures, Rai and Yu referenced the findings of Takata[45–47]: oxygen ions exist stably in the form of O_2^- when the sensing temperature is lower than 100°C (1), as O^- on a ZnO surface when the sensing temperature is 100–300°C (2), and again as O_2^- on the ZnO surface when the sensing temperature is higher than 300°C (3). The CO and oxygen reaction formulae are:

$$2CO(g) + O_2^-(ads) \rightarrow 2CO_2(g) + e^- \tag{1}$$

$$CO(g) + O^-(ads) \rightarrow CO_2(g) + e^- \tag{2}$$

$$CO(g) + O_2^-(ads) \rightarrow CO_2(g) + 2e^- \tag{3}$$

In the third reaction formula, when CO reacts with the oxygen ions, more electrons are released, which causes an increase in current or decrease in impedance to become more evident. The response value also increases as a result. However, situations that require higher sensing temperatures are not conducive to the continued use of sensor components.[48–50] Consequently, the main goal of this study was to develop a gas sensor that can perform in lower temperatures and maintain its response value. ZnO materials have received attention in research on gas sensor chips because of their favorable optical and electrical properties, low cost, and relative lack of harm to the environment. Incorporating an appropriate amount of aluminum can form a heterostructure with ZnO and provide carriers to improve the structure and morphology of the energy band.[51–53] These changes in turn help to increase the reaction sensitivity and response value of the film to CO. In addition, the sputtering process enables the creation of thinner films and more precise control of film thickness than does the chemical bath deposition used in other studies. This creation process can also be conducted at lower temperatures and is therefore more likely to be applied to flexible components and devices. Therefore, this study used radiofrequency (RF) magnetron sputtering to deposit AZO nanofilms with various powers to modulate the surface morphology. Various amounts of oxygen were introduced during deposition to alter the concentration of the oxygen vacancies (V_O) in the film.[54–56] The purpose of modulating the porousness of the film surface was to identify the AZO nanofilm surface structure with the greatest surface absorbance area and to increase the sensitivity of the CO-sensing elements.

Experiment Process

Gas sensor analysis was directly performed on 1 cm × 1 cm × 0.2 mm glass substrates under a working temperature of 100°C. The AZO target was ZnO doped with 2 wt% Al_2O_3 and radio frequency magnetron sputtering was used to deposit thin films. After cleaning, the glass substrates and were placed on platforms in a chamber, the background pressure of which was 3.75×10^{-4} kPa. The working gases pumped into the chamber were argon and oxygen; the argon was 15 sccm, and the oxygen flux alternated between 0, 10, and 15 sccm. Various amounts of oxygen flux were used to adjust the V_O concentration in the film and the porousness of the film surface. The deposition of the AZO film was performed for 1 h at a fixed power of 150 W. After deposition, sensor film packaging was performed to facilitate gas sensing. The gas sensor film was placed on a heating platform within a vacuum sphere, and crocodile clips were used to secure and connect four wires to the power supply, a Keithley 2400. Nitrogen and the target gas—in this case, CO—were introduced to the vacuum sphere to perform gas sensing at a working temperature of 100°C. The Keithley 2400 was used to perform real-time impedance monitoring while the gas-sensing response values were measured. After the optimal oxygen flux was identified, the power of the film deposition was altered to 125 W, 150 W, and 175 W to modulate the porousness of the AZO film surface. The working gas amounts were 15 sccm argon and 10 sccm nitrogen, and sputtering was conducted for 1 h. Scanning electron microscopy (SEM) and x-ray diffractometry (XRD) were used to analyze the porousness, crystallinity, and grain size of the film surface. Ultraviolet–visible (UV-Vis) spectrometry was used to analyze the absorbance rate of the film and to provide indirect insight into the porous properties of the film surface. These measurements were analyzed to determine the optimal parameters of oxygen flux and sputtering power. Finally, to determine the optimal working temperature range, the working sensor temperature was changed to 90°C, 95°C, 100°C, and 105°C while the gas-sensing data were measured and analyzed.

Results and Discussion

Figure 1a, b and c shows the impedance in the AZO nanofilms during CO sensing when oxygen flux was 0, 10, and 15 sccm, respectively. All three films reacted to CO and exhibited decreases in impedance after CO was introduced. The lowest impedance was observed at 270 s when the oxygen flux was 10 sccm and at 300 s when the oxygen flux was 0 or 15 sccm. When CO was introduced, the film produced using an oxygen flux of 10 sccm showed the fastest impedance drop. This shows that, when the oxygen flux is 10 sccm, the
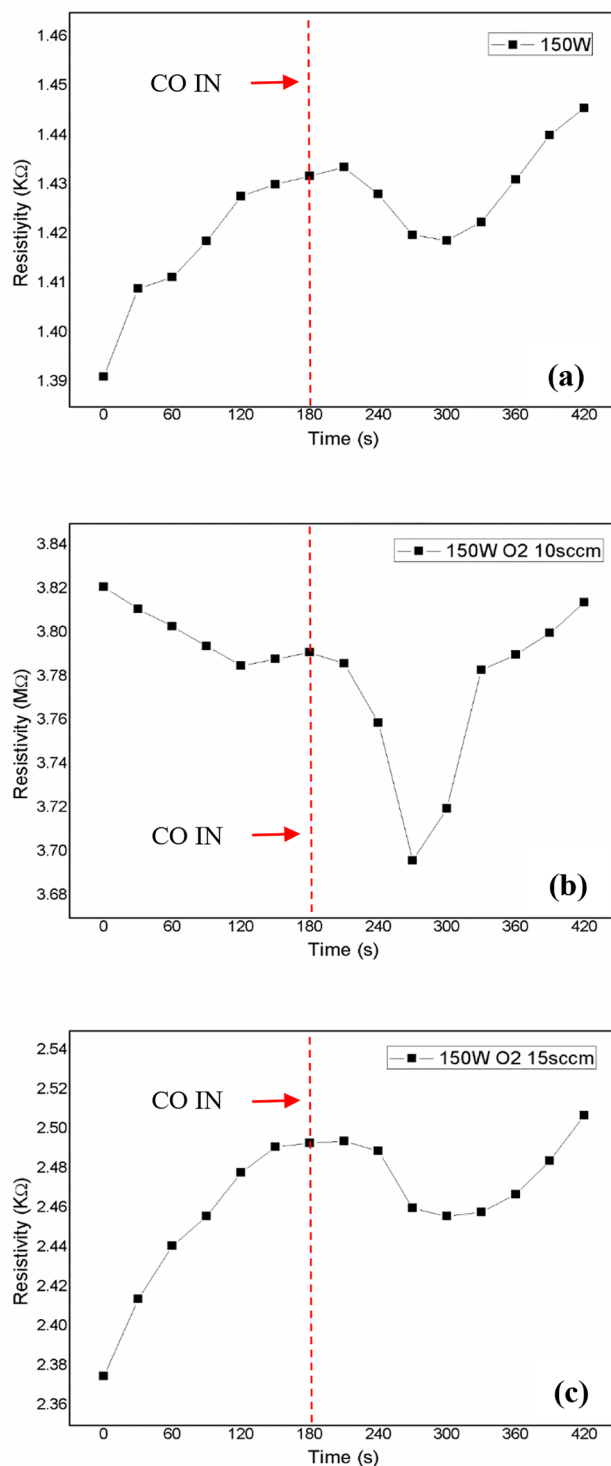

Fig. 1 Resistivity change rate of AZO films during CO sensing over time: (a) no oxygen flux, (b) 10 sccm, (c) 15 sccm.

surface morphology of the AZO film shows higher sensitivity. Table I presents the highest CO response values of the AZO thin films with various amounts of oxygen flux. Thin film with an oxygen flux of 10 sccm not only exhibited faster
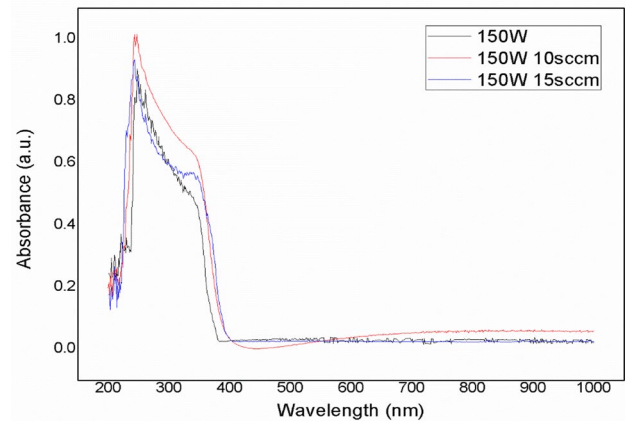
Table 1 Response values of AZO thin films during CO sensing with various oxygen flux

Oxygen flux	R_a (Ω)	R_g (Ω)	$S = R_a/R_g$
0 sccm	1.4318 K	1.4187 K	1.009
10 sccm	3.791 M	3.696 M	1.026
15 sccm	2.493 K	2.456 K	1.015

Fig. 2 Response values of AZO films during CO sensing with various oxygen flux.
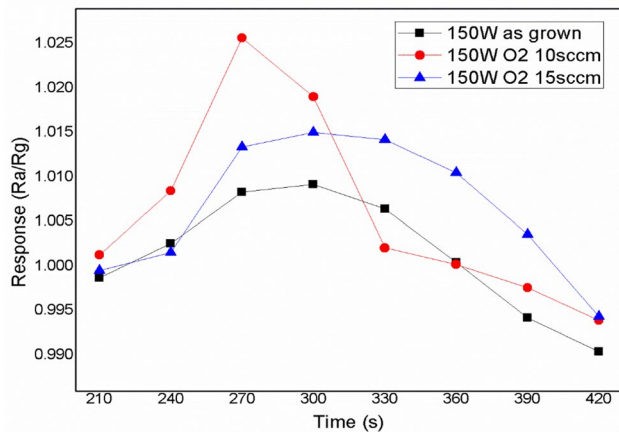
Fig. 3 Light absorbance of AZO thin films surface with various oxygen flux.

response speeds but also the highest CO response values. Figure 2 shows the CO response values of the AZO thin films at different time intervals. The 10-sccm oxygen flux films outperformed the 0- and 15-sccm oxygen flux films in terms of response sensitivity and response values. Analysis of the CO-sensing properties of the AZO thin films revealed that the 10-sccm oxygen flux resulted in a response value of 1.0257, the highest parameter at this stage of the process. In the subsequent processes, the oxygen flux was fixed to 10 sccm, and the sputtering power was modulated to study its effects on film surface morphology.

The optical energy band of ZnO materials is approximately 3.37 eV wide, which is in the wavelength range of ultraviolet light. Light absorbance by the AZO film was measured using UV-Vis spectrophotometry; the UV light-absorbing properties of the film can indirectly reveal the porousness of the film surface. Figure 3 shows the optical absorbance of AZO films under different oxygen fluxes. Films with oxygen fluxes of 0 and 15 sccm have similar light absorption rates, while films with oxygen flux of 10 sccm exhibit higher light absorption rates. These results are consistent with the analysis of the CO-sensing properties of AZO films, showing that the 10-sccm oxygen flux film has higher surface porosity than the 0- and 15-sccm films, making it favorable for gas reactions. As part of the examination of the effects of different oxygen flux amounts on the surface structure and morphology of the AZO thin film, top and cross-sectional views of the thin film were taken through SEM after oxygen flux processing. Figure 4a, b, and c presents the SEM top view of the AZO films. The thin film with 0-sccm oxygen flux had larger grain sizes than did the thin films with 10- and 15-sccm oxygen flux, and the grain size of the thin film decreased with the introduction of oxygen. When the oxygen flux was 10 sccm, the grain size of the thin film shrank considerably, but some larger grains remained. The gaps between the particles increased because of the small granules. Increasing the oxygen flux to 15 sccm did not lead to noticeable changes in grain size, but the sporadically appearing larger grains disappeared; the main difference between the two oxygen flux amounts was that the 15-sccm oxygen flux film had more evenly sized grains. Figure 4d, e and f presents the SEM cross-sectional images of the thin films of different oxygen flux amounts. The 50-K magnification of the SEM image reveals that, when the oxygen flux was 0 sccm, the thin film had a thickness of 550 nm and a compact columnar structure. Cross-sections indicate a smooth surface. When the oxygen flux was 10 sccm, the thickness of the film was lower, therefore, the SEM magnification was increased to 100 K to reveal larger particles and more pores on the film surface. When the oxygen flux was 15 sccm, the film thickness was consistent, and the lack of noticeably larger particles resulted in a flat film surface.

The purpose of modulating oxygen flux was to alter the V_O of the AZO thin film, which simultaneously affects the rate of film deposition. The further increase in oxygen flux also led to a noticeable decrease in the film deposition rate because the influx of oxygen chemically attaches to the surface of the target to form an oxygen absorbance layer, which inhibits the sputtering of atoms on the target surface and results in slower deposition. In addition, because oxygen has lower ionization energy than does argon, when the oxygen
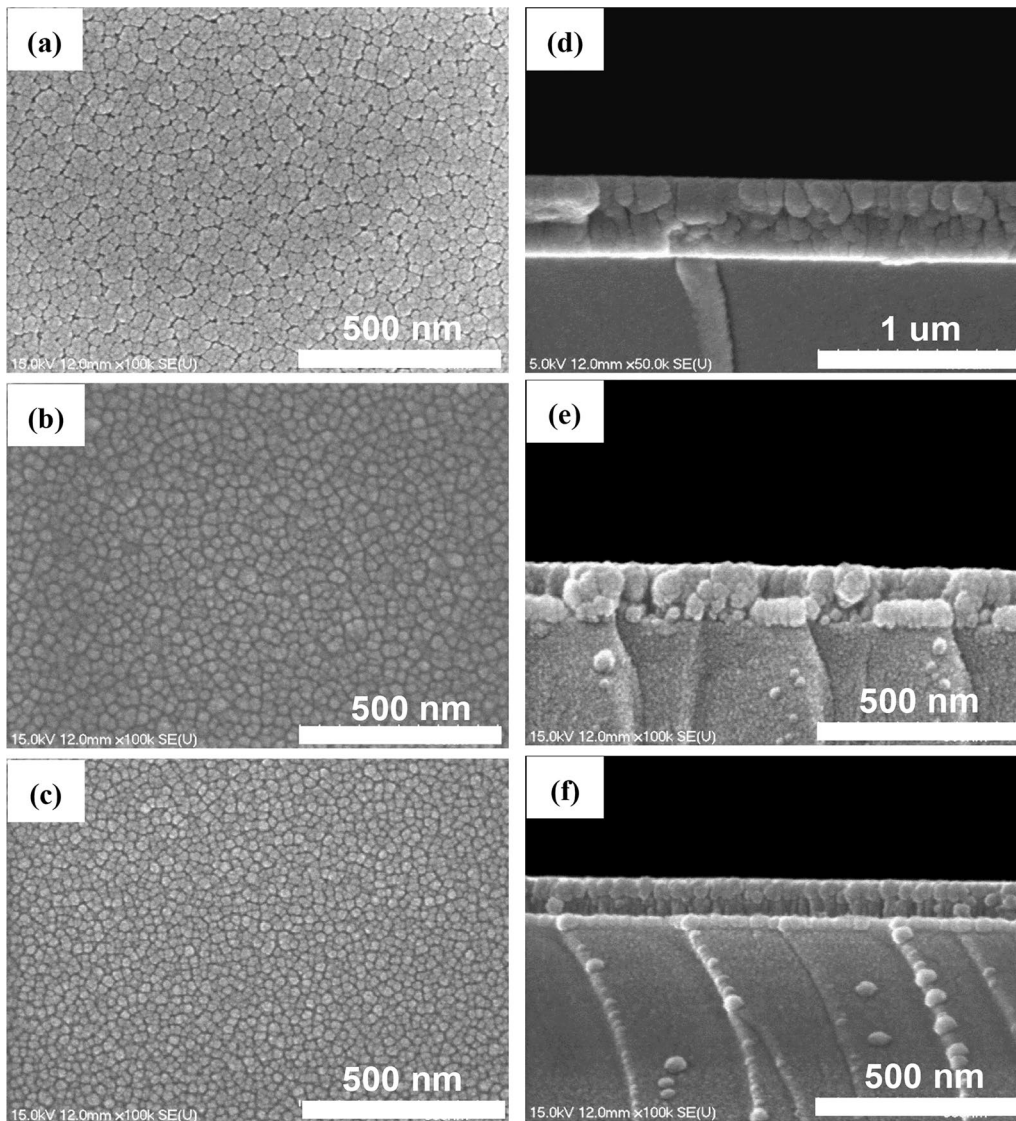
Fig. 4 SEM images of AZO thin films with different oxygen flux: top views from (a) 0 sccm, (b) 10 sccm, (c) 15 sccm; cross-section views from (d) 0 sccm, (e) 10 sccm, (f) 15 sccm.

flux increases, the number of argon ions in the sputtering environment decreases; as a result, the sputtering speed also decreases. The microstructural analysis demonstrated that introducing oxygen during deposition can produce changes in the surface structure of the thin films and increase their porousness. SEM demonstrated that an oxygen flux of 10 sccm is the most appropriate parameter for this stage of the processing. The power of the sputtering was modulated to optimize the surface morphology of the thin films for CO sensors.

Figure 5 presents the XRD graph of the AZO films with different oxygen flux amounts. The main diffraction maximum in the lines represents the main direction of crystallization. At 2θ, 33.6° and 62.8° were the preferred directions for (002) and (103) in ZnO, respectively, with (002)

exhibiting a more prominent characteristic diffraction peak. The graph demonstrates that thin films deposited through an oxygen flux process have less intense main diffraction peaks than do thin films deposited without oxygen flux, revealing that introducing oxygen during the sputtering process results in thin films with low crystallinity. When oxygen was not introduced to the sputtering process, the resulting thin films had the highest main diffraction maximum and the lowest full width at half-maximum (FWHM) at 0.42. The lower the FWHM, the larger the crystals on the surface of the thin film. The average grain size of the thin film with no oxygen flux was 20 nm. These data demonstrated that an oxygen flux of 0 resulted in the best thin film crystallinity, that is, with the minimum defects in internal structure and compact deposition. However, the porousness of the thin
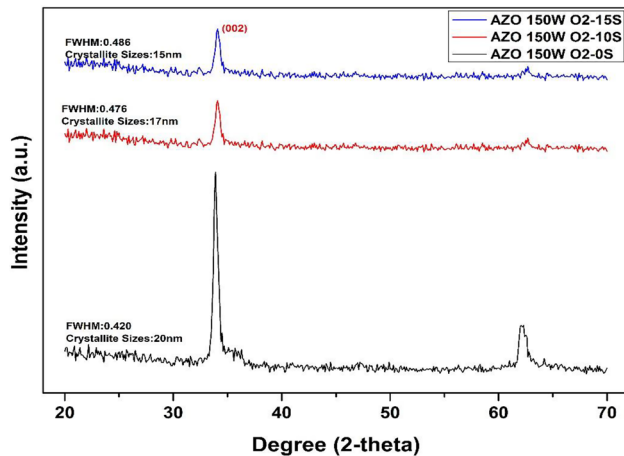
Fig. 5 XRD spectra of AZO thin films with various oxygen flux.

film was also low, which reduced its applicability for gas sensing. When 10 sccm of oxygen was introduced during the sputtering process, the main diffraction maximum noticeably decreased, indicating that the introduction of oxygen decreased crystallinity and increased the FWHM from 0.42 to 0.476. The average grain size also decreased from 20 nm to 17 nm. When the oxygen flux was increased to 15 sccm, the main diffraction peak was similar to that of the thin film with an oxygen flux of 10 sccm, and the FWHM increased slightly, from 0.476 to 0.486. This thin film also had the smallest grain size, which was 15 nm on average. Analysis of the crystalline properties of the thin film revealed that introducing oxygen to the sputtering process not only alters the oxygen vacancies in the thin film structure but also the oxygen chemically attaches to the surface of the target to form an oxygen absorbance layer. This layer inhibits the sputtering of atoms on the target surface, slowing deposition. Increasing the oxygen flux results in an increase of the FWHM and a reduction in the main diffraction peak and average grain size. A reduction in grain size is consistent with the literature[38] and can increase the reaction of the thin films to gas and therefore the gas-sensing response value, indicating that introducing oxygen during the sputtering process not only alters the oxygen vacancies in the film structure and slows deposition but also alters the CO-sensing properties of the thin film by affecting porousness and crystallinity. At this stage, although the 15-sccm oxygen flux resulted in the smallest grain size, after considering all the measurements, we proceeded to the next stage with 10 sccm as the oxygen flux parameter.

Figure 6a, b, and c shows the change in impedance during CO sensing for the AZO films when the sputtering power was 125 W, 150 W, and 175 W, respectively. All three types of thin films exhibited decreases in impedance as a reaction to the introduction of CO. For all three powers, the
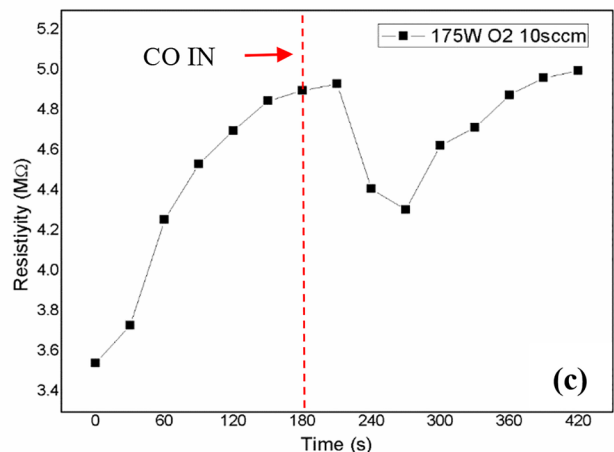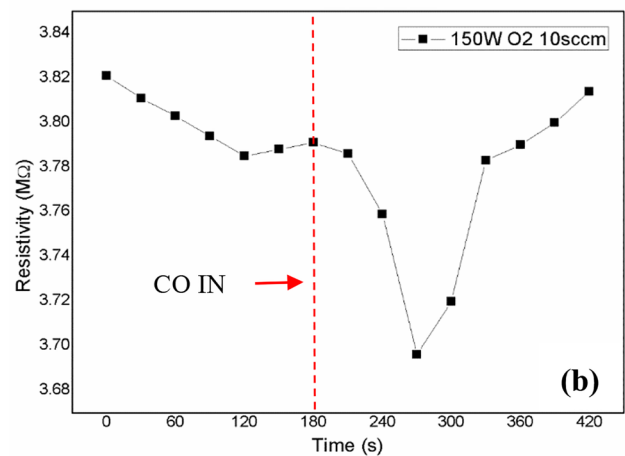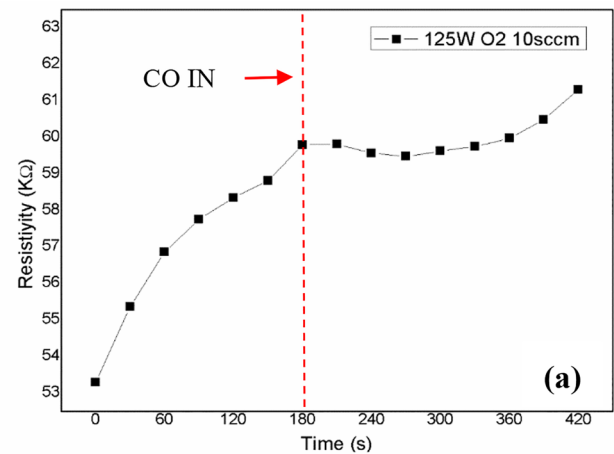

Fig. 6 Resistivity change rate of AZO films during CO sensing with various sputtering powers: (a)125 W, (b)150 W, (c)175 W.
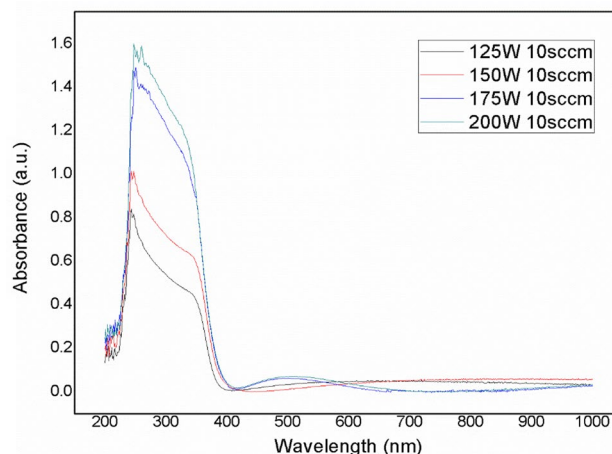
lowest impedance value was observed at 270 s, indicating that all three films had similar reaction speeds. However, the noticeable difference in the decreasing impedance indicates substantial differences in response values. Table II presents

Sputtering power	R_a (Ω)	R_g (Ω)	$S = R_a/R_g$
125 W	59.793 K	59.475 K	1.005
150 W	3.791 M	3.696 M	1.026
175 W	4.9 M	4.307 M	1.138
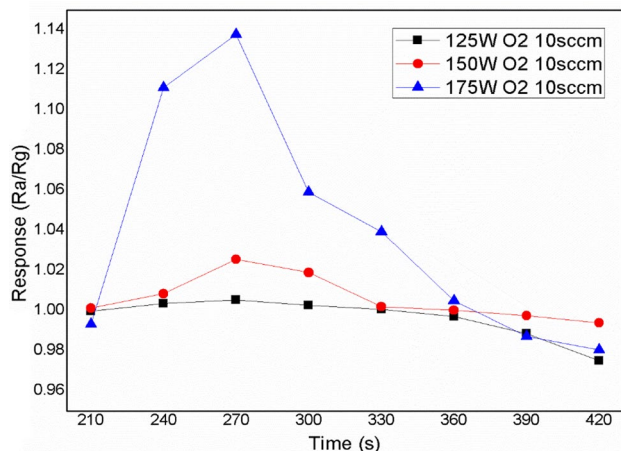
Fig. 7 Response values of AZO films during CO sensing with different sputtering powers.

Fig. 8 Light absorbance of AZO thin films surface with various sputtering powers.

the highest CO-sensing response values of the AZO films by sputtering power. The greatest change in impedance occurred when the power was 175 W; the highest response value also increased by 11% from that when the sputtering power was 150 W. Figure 7 shows the CO-sensing response values over time; 175 W resulted in higher response values than did the other two powers, indicating the optimal reaction duration. Therefore, the sputtering power of 175 W is the most suitable parameter for processing gas-sensitive films at this stage. To further determine the most appropriate power treatment parameters, the super-absorbance of AZO films was analyzed using UV-Vis spectrophotometry to indirectly understand the surface morphology. On the basis of light absorption (Fig. 8), when the power increases, the light absorption of the film also increases. When the power was increased to 175 W, the absorbance was higher than when the power was 150 W; however, there was no significant difference in light absorbance between 175 W and 200 W sputtering power. Figure 9a, b, and c shows the SEM top view of the AZO film when the sputtering power was 125, 150 and 175 W, respectively. When the power is 125 W, the pores in the film are not obvious, the particle size is uneven, and large particles exist. When the sputtering power is 150 W, some larger grains remain on the film surface, but fewer grains are observed on the 125-W film; the surface pores

were also more visible. When the power was increased to 175 W, the surface morphology of the thin film did not differ considerably from that of the 150-W thin film; some larger grains were present, but the overall grain sizes were smaller than those in the 125-W film, and the surface pores visibly increased. The SEM cross-sectional images also demonstrate that, when the sputtering power was increased, the surface pores became more noticeable, and the grain size decreased accordingly. However, differences between sputtering powers of 150 W and 175 W were not easily observed in the analysis of the surface structures of the thin films; the structure of the thin films was determined in the subsequent analysis of crystallinity. Figure 10 presents an XRD graph of the AZO films processed under different sputtering powers. The main diffraction maximum in the lines represent the main direction of crystallization. At 2θ, 33.6° and 62.8° were the preferred directions for (002) and (103) of ZnO, respectively, with (002) as the obvious characteristic diffraction peak. A sputtering power of 125 W resulted in an FWHM of 0.382 and an average grain size of 22 nm. When the sputtering power was increased to 150 W, the main diffraction peak decreased slightly in intensity, whereas the FWHM increased to 0.476. This indicates a reduction in grain size to approximately 17 nm. When the sputtering power was further increased to 175 W, the intensity of the main diffraction peak began to increase slightly, and the FWHM continued to increase to 0.587. The grain size continued to decrease to 15 nm on average, but the shrinkage rate decreased gradually. Increasing the sputtering power to 200 W resulted in a stark increase in the intensity of the main diffraction peak and another visible diffraction peak in the (103) direction. This indicates that a sputtering power of 200 W resulted in thin films with more favorable crystallinity. Despite the slight difference in grain size, the FWHM decreased to

Fig. 10 XRD spectra of AZO thin films with different sputtering powers.
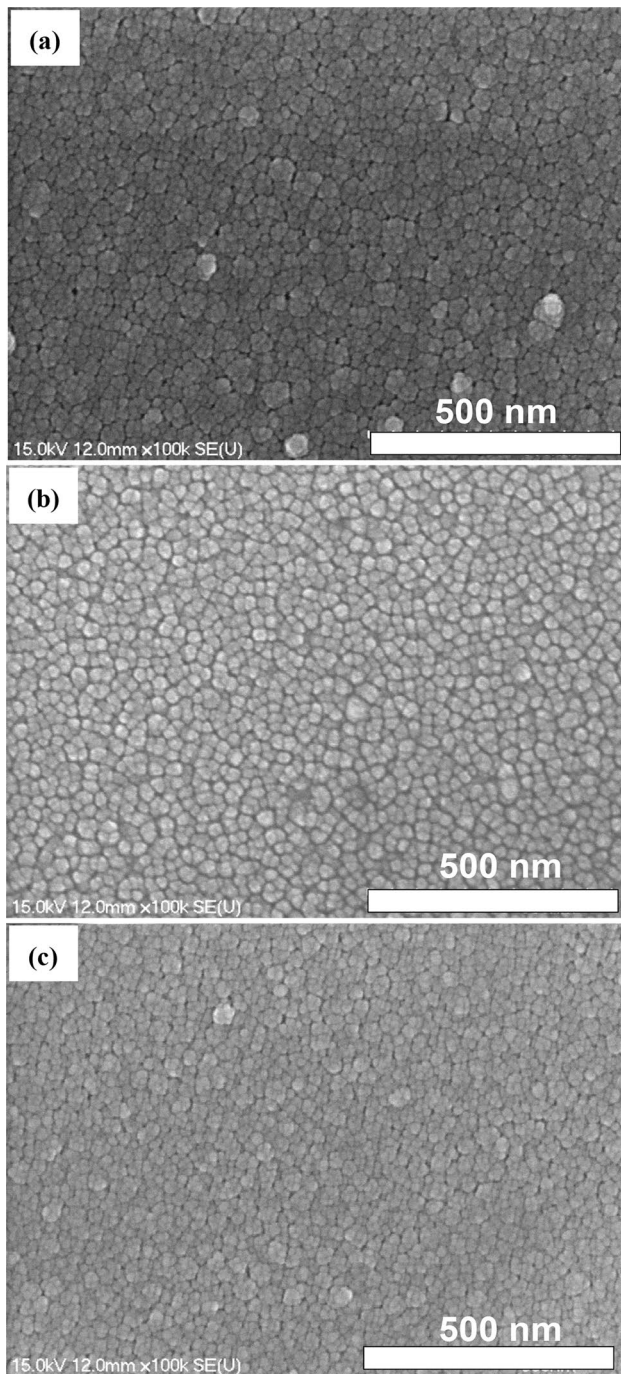
Fig. 9 SEM top view of AZO thin films with different sputtering powers: (a)125 W, (b)150 W, (c)175 W.

0.572, demonstrating an increase in film crystallinity when the sputtering power was 200 W. Increasing the sputtering power resulted in more intense XRD diffraction peaks. Therefore, the increase in crystallinity of AZO films is due to the higher sputtering power, which provides more energy to the argon ions, which then collide with the target surface at a higher speed. As a result, atoms on the film surface have
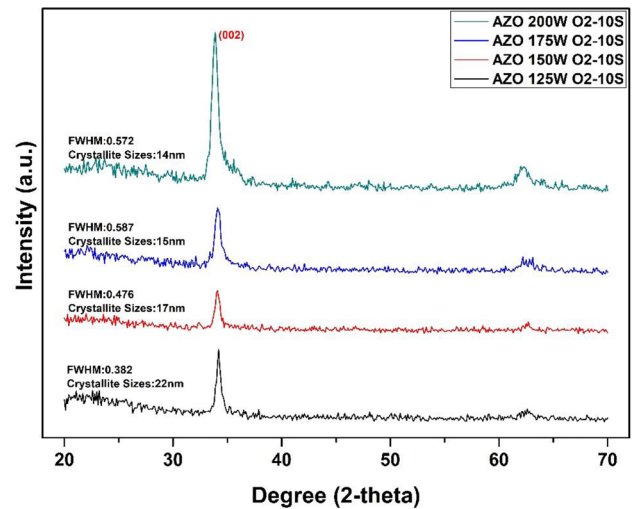
better mobility, thereby increasing the sputtering power and film crystallinity. However, despite the increased crystallinity when the sputtering power was 200 W, the resulting thin film was not suitable for use as a gas detector. The reduction in FWHM indicates an increase in grain size, which does not satisfy the gas-sensing requirements. Although the 150-W film had a slightly lower diffraction peak, the 175-W film had smaller grain sizes, indicating that the 175-W sputtering power was the most suitable for processing sensor films.

Figure 11a, b, c, and d shows the impedance from CO sensing at different working temperatures. In Fig. 11a, which involves a working temperature of 90°C, the impedance increased prior to the introduction of CO and continued to increase until 90 s after CO was introduced. It then decreased slightly, indicating a low response intensity. When the working temperature was increased to 95°C (Fig. 11b), the impedance began to decrease noticeably 60 s after the CO introduction, indicating that, when the temperature slowly increased, the surface of the thin film gradually reacted more intensely to the gas. Figure 11c and d presents working temperatures of 100°C and 105°C, respectively. When the temperature rose to above 100°C, the reactions become visibly more intense. Setting 100°C as the critical reaction temperature led to visible differences in response values (Fig. 12). Studies have typically involved gas-sensing temperatures between 200°C and 400°C, but, because higher working temperatures limit the subsequent application and development of the components, lower working temperatures were used in this experiment. Temperatures of 105°C and 100°C resulted in little difference in sensitivity and response value (Fig. 12). When the temperature dropped below 100°C, the response value decreased substantially; at 95°C,
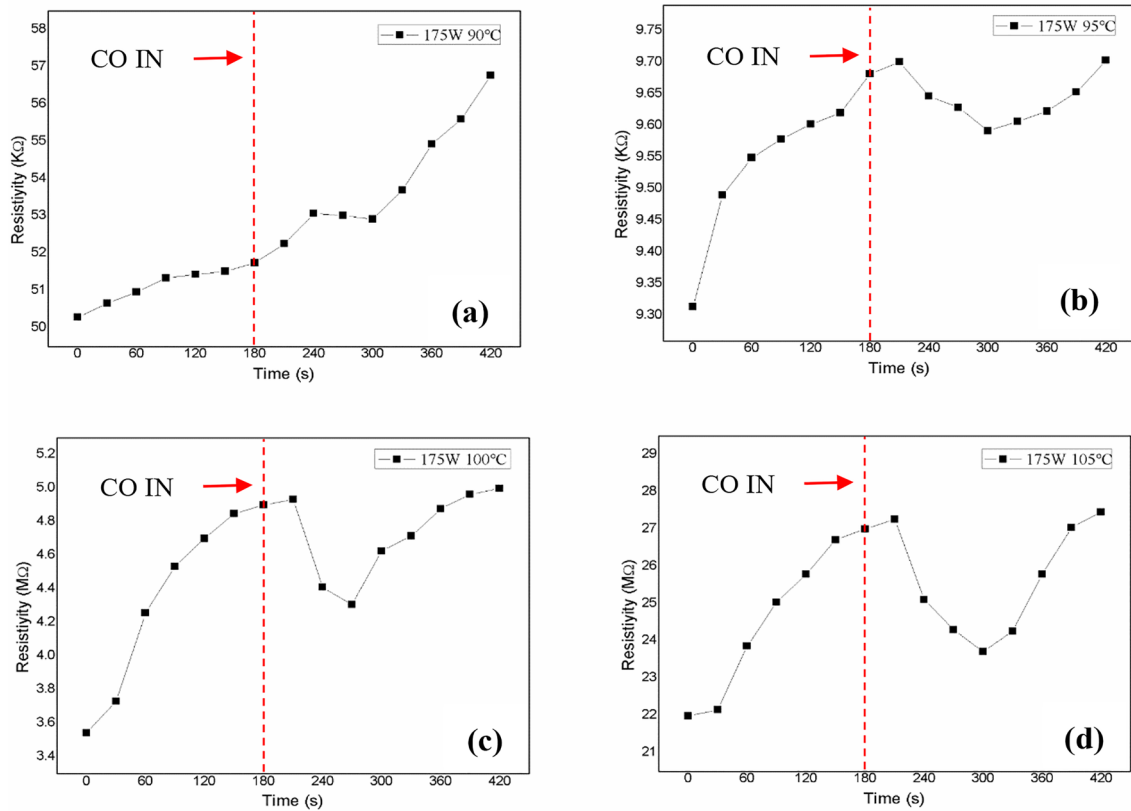
Fig. 11 Resistivity change rate of AZO films during CO sensing under different working temperature: (a) 90°C, (b) 95°C, (c) 100°C, (d) 105°C.
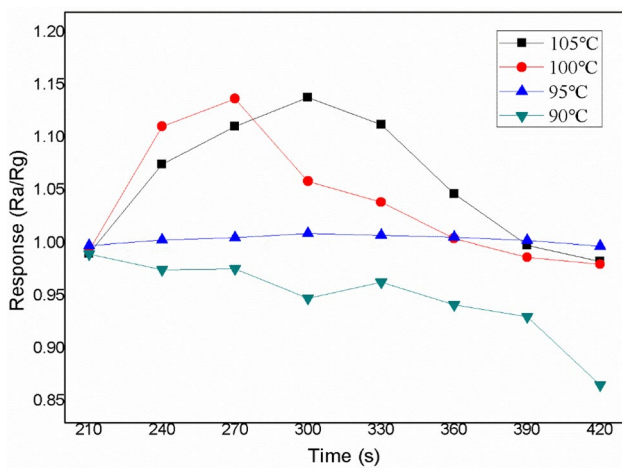
Fig. 12 Response values of AZO films during CO sensing under different working temperatures.

despite the considerable decrease in reaction intensity, the response value remained above 1, and when the temperature decreased to 90°C, the decrease in reaction intensity became even more apparent, and the response value

decreased to less than 1. This result can be attributed to the fact that oxygen on the surface of the film exists stably in different ionic forms at different temperatures. Therefore, the amount of CO consumed as the surface oxygen ions reacted with CO to release one electron when the working temperature was lower than 100°C was twice that when the working temperature was 100–300°C, as demonstrated by:

$$2CO_{(g)} + O^-_{2(ads)} \rightarrow 2CO_{2(g)} + e^- \tag{4}$$

$$CO_{(g)} + O^-_{(ads)} \rightarrow CO_{2(g)} + e^- \tag{5}$$
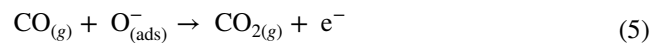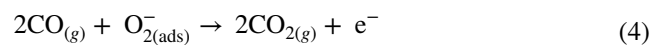
On the basis of the change in impedance exhibited by the AZO thin films under different working temperatures, lower temperatures affect the intensity of the reaction between the thin film surface and the gas. In addition, lowering the temperature to below 100°C causes the reaction intensity to decrease by a considerably larger magnitude, which is due to the different stable forms of oxygen ions on the film surface. An analysis of the feasibility of the gas sensors in lower working temperatures revealed that 100°C is the critical working temperature in gas sensing.

Conclusions

Thin films deposited by RF magnetron sputtering were applied to gas sensing, Oxygen flux and sputtering power were altered to increase the porousness of the thin film surface for use in a CO sensor. The optimal parameters for depositing AZO thin films were determined to be an oxygen flux of 10 sccm and a sputtering power of 175 W. These parameters produced maximum response values of 1.138, a 13% increase from that without treatment. This indicates that introducing oxygen to the sputtering process and increasing the power appropriately can increase the porousness of the thin film surface, which increases the gas-sensing response value. In addition, the working temperature is critical to gas sensing. Compared with other studies, this study achieved gas-sensing properties at operating temperatures as low as 100°C. The designed AZO thin films were deposited by RF magnetron sputtering, which demonstrated the films' potential application in gas sensors. Regarding the lower operating temperature in this study, a more in-depth analysis of the film microstructure after the optimized process has been conducted will provide further explanations in future publications.

Author contributions Y-SL and S-HS conceived and designed the experiments. S-HH, Y-ZA and J-SH performed the experiments and collected the measurement data. Y-SL and S-HS analyzed the data and plotted the figures. Y-SL polished the figures, wrote and polished the paper.

Data availability The datasets generated during and/or analyzed during the current study are available from the corresponding author on request.

Conflict of interest The authors declare that they have no conflict of interest.

References

1. A. Dey, Semiconductor metal oxide gas sensors. *Mater. Sci. Eng. B* 229, 206 (2018).
2. J. Kong, N.R. Franklin, C. Zhou, M.G. Chapline, S. Peng, K. Cho, and H. Dai, Nanotube molecular wires as chemical sensors. *Science* 287, 622 (2000).
3. C.S. Rout, A.R. Raju, A. Govindaraj, and C.N.R. Rao, Hydrogen sensors based on ZnO nanoparticles. *Solid State Commun.* 138, 136 (2006).
4. Y.-J. Chen, C.-L. Zhub, and G. Xiao, Ethanol sensing characteristics of ambient temperature sonochemically synthesized ZnO nanotubes. *Sens. Actuators B* 129, 639 (2008).
5. Xu. Jiaqiang, C. Yuping, C. Daoyong, and S. Jianian, Hydrothermal synthesis and gas sensing characters of ZnO nanorods. *Sens. Actuators B* 113, 526 (2006).
6. S. Choopun, N. Hongsith, P. Mangkorntong, and N. Mangkorntong, Zinc oxide nanobelts by RF sputtering for ethanol sensor. *Phys. E* 39, 53 (2007).
7. J. Liu, Z. Guo, T.L. FanliMeng, M. Li, and J. Liu, Novel porous single-crystalline ZnO nanosheets fabricated by annealing ZnS(en)05 (en = ethylenediamine) precursor Application in a gas sensor for indoor air contaminant detection. *Nanotechnology* 20, 125501 (2009).
8. T.M. Perfecto, C.A. Zito, and D.P. Volanti, Effect of NiS nanosheets on the butanone sensing performance of ZnO hollow spheres under humidity conditions. *Sens. Actuators B* 334, 129684 (2021).
9. I. Karaduman Er, I.A. Yildiz, T. Bayraktar, S. Acar, and A. Ateş, The dependence of the gas sensing properties of ZnO thin films on the zinc concentration. *J. Mater. Sci.: Mater. Electr.* 32, 8122–8135 (2021).
10. Su. Xingsong, G. Duana, Xu. Zongke, F. Zhoua, and W. Cai, Structure and thickness-dependent gas sensing responses to NO2 under UV irradiation for the multilayered ZnO micro/nanostructured porous thin films. *J. Colloid Interface Sci.* 503, 150 (2017).
11. F.T. Mackenzie, and J.A. Mackenzie, *Our changing planet* (Upper Saddle River: Prentice-Hall, 1995), p.288.
12. D. Van Dao, T.T.D. Nguyen, S.M. Majhi, G. Adilbish, H.J. Lee, Y. Yeon-Tae, and I.H. Lee, Ionic liquid-supported synthesis of CeO_2 nanoparticles and its enhanced ethanol gas sensing properties. *Mater. Chem. Phys.* 231, 1 (2019).
13. P. Werle, F. Slemr, K. Maurer, R. Kormann, R. Mücke, and B. Jänker, Near-and mid-infrared laser-optical sensors for gas analysis. *Opt. Lasers Eng.* 37(2–3), 101–114 (2002).
14. I. Eisele, T. Doll, and M. Burgmair, Low power gas detection with FET sensors. *Sens. Actuators B* 78, 19 (2001).
15. H. Wan, Lu. Heyu Yin, X.Z. Lin, and A.J. Mason, Miniaturized planar room temperature ionic liquid electrochemical gas sensor for rapid multiple gas pollutants monitoring. *Sens. Actuators B* 255, 638 (2018).
16. T. Ueda, T. Defferriere, T. Hyodo, Y. Shimizu, and H.L. Tuller, Nanostructured Pr-doped Ceria (PCO) thin films as sensing electrodes in solid-electrolyte type gas sensors with enhanced toluene sensitivity. *Sens. Actuators B* 317, 128037 (2020).
17. Wu. Meile, J. Shin, Y. Hong, D. Jang, X. Jin, H.-I. Kwon, and J.-H. Lee, An FET-type gas sensor with a sodium ion conducting solid electrolyte for CO2 detection. *Sens. Actuators B* 259, 1058 (2018).
18. T. Ueda, H. Abe, K. Kamada, S.R. Bishop, H.L. Tuller, T. Hyodo, and Y. Shimizu, Enhanced sensing response of solid-electrolyte gas sensors to toluene: role of composite Au/metal oxide sensing electrode. *Sens. Actuators B* 252, 268 (2017).
19. L. Talazac, J. Brunet, V. Battut, J.P. Blanc, A. Pauly, J.P. Germain, S. Pellier, and C. Soulier, Air quality evaluation by monolithic InP-based resistive sensors. *Sens. Actuators B* 76, 258 (2001).
20. B. Adhikari, and S. Majumdar, Polymers in sensor applications. *Prog. Polym. Sci.* 29, 699 (2004).
21. Z. Zhou, Xu. Yongzheng, C. Qiao, L. Liu, and Y. Jia, A novel low-cost gas sensor for CO_2 detection using polymer-coated fiber Bragg grating. *Sens. Actuators B* 332, 129482 (2021).
22. D. Zhang, Wu. Zhenling, and X. Zong, Flexible and highly sensitive H_2S gas sensor based on in-situ polymerized SnO_2/rGO/PANI ternary nanocomposite with application in halitosis diagnosis. *Sens. Actuators B* 289, 32 (2019).
23. J. He, B. Liang, X. Yan, F. Liu, J. Wang, Z. Yang, R. You, C. Wang, Xu. Peng Sun, H.L. Yan, B. Kang, Y. Wang, and Lu. Geyu, A TPA-DCPP organic semiconductor film-based room

temperature NH3 sensor for insight into the sensing properties. *Sens. Actuators B* 327, 128940 (2021).

24. G. Korotcenkov, Gas response control through structural and chemical modification of metal oxide films: state of the art and approaches. *Sens. Actuators B* 107, 209 (2005).

25. P. Cao, Z. Yang, S.T. Navale, S. Han, X. Liu, W. Liu, Y. Lu, F.J. Stadler, and D. Zhu, Ethanol sensing behavior of Pd-nanoparticles decorated ZnO-nanorod based chemiresistive gas sensors. *Sens. Actuators B: Chem.* 1(298), 126850 (2019).

26. J.-H. Lee, J.-Y. Kim, J.-H. Kim, and A. Mirzaei, Hyoun Woo Kim, Sang Sub Kim, Pd-decorated Si nano-horns as sensitive and selective hydrogen gas sensors. *Mater. Res. Bull.* 132, 110985 (2020).

27. J. Chao, Z. Liu, S. Xing, Q. Gao, and J. Zhao, Conductometric room temperature ammonia sensors based on titanium dioxide nanoparticles decorated thin black phosphorus nanosheets. *Sens. Actuators B* 347, 130621 (2021).

28. Y. Wang, Y. Cui, X. Meng, Z. Zhang, and J. Cao, A gas sensor based on Ag-modified ZnO flower-like microspheres: temperature-modulated dual selectivity to CO and CH$_4$. *Surf. Interfaces* 24, 101110 (2021).

29. P.J. Shaver, Activated tungsten oxide gas detectors. *Appl. Phys. Lett.* 11, 255 (1967).

30. C.-Y. Chi, H.-I. Chen, W.-C. Chen, C.-H. Chang, and W.-C. Liu, Formaldehyde sensing characteristics of an aluminum-doped zinc oxide (AZO) thin-film-based sensor. *Sens. Actuators B* 255, 3017 (2018).

31. V. VasanthiPillay, Sarita goyal, influence of sputtering power, annealing on the structural properties of ITO Films, for application in ethanol gas sensor. *Mater. Today: Proc.* 2, 4609 (2015).

32. A.S. Mokrushin, N.A. Fisenko, P.Y. Gorobtsov, T.L. Simonenko, O.V. Glumov, N.A. Melnikova, N.P. Simonenko, K.A. Bukunov, E.P. Simonenko, V.G. Sevastyanov, and N.T. Kuznetsov, Pen plotter printing of ITO thin film as a highly CO sensitive component of a resistive gas sensor. *Talanta* 1(221), 121455 (2021).

33. Y. Kang, Yu. Feng, Lu. Zhang, W. Wang, L. Chen, and Y. Li, Review of ZnO-based nanomaterials in gas sensors. *Solid State Ion.* 360, 115544 (2021).

34. U.T. Nakate, G.H. Lee, R. Ahmad, P. Patil, Y.B. Hahn, Y.T. Yu, and E.K. Suh, Nano-bitter gourd like structured CuO for enhanced hydrogen gas sensor application. *Int. J. Hydrog. Energy* 43(50), 22705–22714 (2018).

35. J. Wang, H. Shen, Yi. Xia, and S. Komarnen, Light-activated room-temperature gas sensors based on metal oxide nanostructures: a review on recent advances. *Ceram. Int.* 47, 7353 (2021).

36. Xu. Chaonan, J. Tamaki, N. Miura, and N. Yamazoe, Grain size effects on gas sensitivity of porous SnO2-based elements. *Sens. Actuators B* 3, 147 (1991).

37. P. Rai, and Yu. Yeon-Tae, Synthesis of floral assembly with single crystalline ZnO nanorods and its CO sensing property. *Sens. Actuators B* 161, 748 (2012).

38. B. Yang, C. Yao, Y. Yu, Z. Li, and X. Wang, Nature degradable, flexible, and transparent conductive substrates from green and earth-abundant materials. *Materials. Sci. Rep.* 7, 4936 (2017).

39. X. Zhang, W. Wang, D. Zhang, M. Qian, and Y. Sujing, Self-powered ethanol gas sensor based on the piezoelectric Ag/ZnO nanowire arrays at room temperature. *J. Mater. Sci. Mater. Electron.* 32, 7739 (2021).

40. T. Pauporte, O. Lupan, J. Zhang, T. Tugsuz, I. Ciofifini, and F. Labat, Low-temperature preparation of Ag-Doped ZnO nanowire arrays, DFT study, and application to light-emitting diode. *ACS Appl. Mater. Interfaces* 7, 11871 (2015).

41. D. Zhang, Z. Yang, Z. Wu, and G. Dong, Metal-organic frameworks-derived hollow zinc oxide/cobalt oxide nanoheterostructure for highly sensitive acetone sensing. *Sens. Actuators B* 283, 42 (2019).

42. A. Janotti, and C.G. Van de Walle, Fundamentals of zinc oxide as a semiconductor. *Rep. Prog. Phys.* 72(126501), 29 (2009).

43. L.W. Zhong, Zinc oxide nanostructures: growth, properties and applications. *J. Phys. Condens. Matter* 16, R829 (2004).

44. D.L. Raimondi, and E. Kay, High resistivity transparent ZnO thin films. *J. Vac. Sci. Technol.* 7, 96 (1970).

45. G.A. Hirata, J. Mckittrik, T. Cheeks, J.M. Siqueiros, J.A. Diaz, O. Contreras, and O.A. Lopez, Synthesis and optelectronic characterization of gallium doped zinc oxide transparent electrodes. *Thin Solid Films* 288, 29 (1996).

46. T. Minami, H. Sato, H. Nanto, and S. Takata, Highly conductive and transparent silicon doped zinc oxide thin films prepared by RF magnetron sputtering. *Jpn. J. Appl. Phys.* 25, 776 (1986).

47. K. Tominaga, and M. Kataoka, Transparent ZnO: Al films prepared by co-sputtering of ZnO: Al with either a Zn or an Al target. *Thin Solid Films* 290–291, 84 (1996).

48. X. Hao, J. Ma, D. Zhang, T. Yang, H. Ma, Y. Yang, C. Cheng, and J. Huang, Thickness dependence of structural, optical and electrical properties of ZnO: Al films prepared on flexible substrates. *Appl. Surf. Sci.* 183(1–2), 137 (2001).

49. K.C. Park, D.Y. Ma, and K.H. Kim, The physical properties of Al-doped zinc oxide films prepared by RF magnetron. *Thin Solid Films* 305, 201 (1997).

50. J.J. Lu, Y.M. Lu, S.I. Tasi, T.L. Hsiung, H.P. Wang, and L.Y. Jang, Conductivity enhancement and semiconductor–metal transition in Ti-doped ZnO films. *Opt. Mater.* 29, 1548 (2007).

51. Y. Igasaki, and H. Saito, The effects of zinc diffusion on the electrical and optical properties of ZnO: Al films prepared by r.f. reactive sputtering. *Thin Solid Films* 199, 223 (1991).

52. D. Dimitrov, C.-L. Tsai, S. Petrov, V. Marinova, D. Petrova, B. Napoleonov, B. Blagoev, V. Strijkova, K.Y. Hsu, and S.H. Lin, Atomic layer-deposited Al-doped ZnO thin films for display applications. *Coatings* 10, 539 (2020).

53. S.R. Dhage, and A.C. Badgujar, Transparent conducting Al:ZnO thin films on large area by efficient cylindrical rotating DC magnetron sputtering. *J. Alloys Compd.* 763, 504–511 (2018).

54. J. Kim, and K. Yong, Mechanism Study of ZnO Nanorod-Bundle Sensors for H2S Gas Sensing. *J. Phys. Chem.* 115, 7218 (2011).

55. R. Zhang, S.Y. Ma, J.L. Zhang, B.J. Wang, and S.T. Pei, Enhanced formaldehyde gas sensing performance based on Bi doped Zn2SnO4/SnO2 porous nanospheres. *J. Alloy. Compd.* 828, 154408 (2020).

56. B. Abdallah, A.K. Jazmati, and R. Refaai, Oxygen effect on structural and optical properties of ZnO thin films deposited by RF magnetron sputtering. *Mater. Res.* 20(3), 607 (2017).